

Internal Stress Evolution and Subsurface Phase Transformation in Titanium Parts Manufactured by Laser Powder Bed Fusion—An In Situ X-Ray Diffraction Study

Felix Schmeiser,* Erwin Krohmer, Norbert Schell, Eckart Uhlmann, and Walter Reimers

Laser powder bed fusion (LPBF) is a metal additive manufacturing technology, which enables the manufacturing of complex geometries for various metals and alloys. Herein, parts made from commercially pure titanium are studied using in situ synchrotron radiation diffraction experiments. Both the phase transformation and the internal stress buildup are evaluated depending on the processing parameters. For this purpose, evaluation approaches for both temperature and internal stresses from in situ diffraction patterns are presented. Four different parameter sets with varying energy inputs and laser scanning strategies are investigated. A combination of a low laser power and scanning speed leads to a more homogeneous stress distribution in the observed gauge volumes. The results show that the phase transformation is triggered during the primary melting and solidification of the powder and subsurface layers. Furthermore, the stress buildup as a function of the part height during the manufacturing process is clarified. A stress maximum is formed below the part surface, extending into deeper layers with increasing laser power. A temperature evaluation approach for absolute internal stresses shows that directional stresses decrease sharply during laser impact and reach their previous magnitude again during cooling.

1. Introduction

Additive manufacturing technologies offer vast possibilities for lightweight design, which appeal to medical and aerospace engineering fields, among other industry branches. In the case of metal part production, laser powder bed fusion (LPBF), which is also referred to as selective laser melting (SLM), is one of the most widely used additive manufacturing technologies due to the geometrical freedom in design while benefiting from relatively good mechanical properties in comparison with conventionally manufactured parts.

While industrial sectors such as medical technology and aviation may greatly benefit from the geometric freedom of design, they also impose high quality and safety standards that, to date, often cannot be met by additive manufacturing technologies. A lack of process knowledge and control over LPBF is expressed in the formation of defects and residual stresses that harm


the components' mechanical behavior.^[1,2] In LPBF, a thin layer of metal powder of typically 30–50 μm is deposited on a solid substrate plate and locally melted by a focused laser beam according to the part's cross-sectional model. Subsequently, a new powder layer is deposited and melted, such that a bond is formed with the solidified layers beneath. This procedure is repeated layer by layer until completion of the part. A complex heat flux with steep temperature gradients is generated for every layer, varying with the material, laser scanning parameters,^[3] built height,^[4] part geometry,^[5] and due to heat accumulation within a single layer.^[6] In turn, a complex stress development occurs with several overlapping, stress-inducing mechanisms introduced by Mercelis and Kruth.^[7] The thermal gradient mechanism (TGM) describes how the exposed material is rapidly heated and plasticized during laser–matter interaction. Colder material below inhibits the thermal expansion of the heated material, resulting in compressive stresses. After laser exposure, the material cools down, and the surrounding material hinders its thermal shrinkage. Schmeiser et al.^[8] experimentally showed that the hindered thermal shrinkage has a much stronger influence on in-plane stresses than out-of-plane stresses. Furthermore, they showed that tensile stresses, as described by Mercelis and Kruth,^[7] are formed in the working plane, whereas in the out-of-plane, those tensile stresses result in a transverse contraction.

F. Schmeiser, Prof. W. Reimers
Institute for Materials Science and Technology
Metallic Materials
Technische Universität Berlin
Ernst-Reuter-Platz 1, 10587 Berlin, Germany
E-mail: felix.schmeiser@tu-berlin.de

E. Krohmer, Prof. E. Uhlmann
Institute for Machine Tools and Factory Management (IWF)
Technische Universität Berlin
Pascalstraße 8-9, 10587 Berlin, Germany

Dr. N. Schell
Institute of Materials Physics
Helmholtz-Zentrum Hereon
Max-Planck-Str. 1, 21502 Geesthacht, Germany

Prof. E. Uhlmann
Fraunhofer Institute for Production Systems and Design Technology (IPK)
Pascalstraße 8-9, 10587 Berlin, Germany

 The ORCID identification number(s) for the author(s) of this article can be found under <https://doi.org/10.1002/adem.202001502>.

© 2021 The Authors. Advanced Engineering Materials published by Wiley-VCH GmbH. This is an open access article under the terms of the Creative Commons Attribution License, which permits use, distribution and reproduction in any medium, provided the original work is properly cited.

DOI: 10.1002/adem.202001502

Numerous studies on the influence of laser scanning parameters on residual stress development can be found in the literature and are summarized in the current review articles on residual stresses in LPBF.^[9,10] While researchers agree that the laser scanning parameters significantly influence the residual stresses, different results can be found regarding the degree of impact of the individual parameters.^[11] Mukherjee et al.^[12] deduced from their thermal simulations that low heat input is favorable for reducing thermal strain in the part. Therefore, the laser power should be chosen as low as possible and the scanning speed as high as possible while maintaining good interlayer bonding of the material, which is in line with a study from Ali et al.^[13] They showed that considering a constant energy density level, combinations of lower laser power and higher exposure time result in lower residual stresses for Ti–6Al–4V specimens. However, other research results seemingly showed contradictory findings that residual stresses decrease with increasing laser power.^[14,15]

Further experimental results on additively manufactured 316L parts using neutron diffraction revealed that deflection induced by residual stresses could be reduced using higher ratios of laser power to scanning speed.^[16] The impact of laser scanning parameters on residual stresses also involves the length and sequence of individual scan lines that form the melt track. Studies have shown that shortening the scan vector length reduces residual stresses for simple unidirectional or alternating scan strategies.^[3,17] Moreover, the highest residual stresses occur parallel to the scan vectors.^[3,18–20] However, for more complex scan strategies, such as island scanning again, contradictory results can be found in the literature, concerning the effect of reducing the scan vector length.^[18,21] Xiao et al.^[11] conclude that the complex relationship between laser scanning parameters and residual stress could be the reason for the contradictory parametric effects reported in the literature. Hence, for a profound process understanding, in situ measurement techniques are needed to extend the knowledge about the impact of process parameters on internal stress evolution during the manufacturing process.

Additively manufactured titanium and its alloys are of particular interest to aerospace technology^[22] as well as medical technology^[23] or even for musical instruments.^[24] Titanium goes through a phase transformation at $T = 882^\circ\text{C}$, where the lattice changes from a hexagonally close-packed (hcp) to a body-centered cubic (bcc) lattice. This transformation entails a slight volume contraction.^[25] The two lattices share a lattice plane, the (200) for the α hcp phase, and the (110) for the β bcc phase.

In LPBF, the powder material goes through the phase transformation during laser exposure, as it is melted and solidified as a melting track. Gu et al.^[26] observed the correlation of phase transformation with the scanning speed on commercially pure titanium grade 2. They observed the formation of martensitic α' phase for scanning speeds $v_L \geq 200\text{ mm s}^{-1}$ and a laser power of $P_L = 90\text{ W}$, and the formation of α phase for a scanning speed $v_L = 100\text{ mm s}^{-1}$. These observations are consistent with the studies by Attar et al.^[27] Essentially, the choice of the laser parameters can alter the cooling and solidification rate and, therefore, the resulting microstructure^[28] and phase composition^[26] depending on the processed material.

Phase transformations have been captured by in situ X-ray diffraction experiments by several research groups^[29–31] with

the constraint of observing the top layer of the part, powder bed, or the substrate only. Dye et al.^[32] used neutron diffraction to observe phase transformations and evaluate absolute stresses during the welding of mild steel. An in situ study under LPBF conditions investigating subsurface phase transformations and stress evolution in multilayer parts is missing to date.

In this study, comprehensive in situ X-ray diffraction experiments with synchrotron radiation were carried out to elucidate the phase transformation dynamics and internal stress development in commercially pure titanium grade 1 (cp-Ti) in subsurface layers using a variety of process and laser scanning parameters. A temperature evaluation approach is introduced to present absolute in situ stress values during LPBF for the first time.

2. Results and Discussion

For the experiments' conduction at the P07 beamline^[33] at Deutsches Elektronen-Synchrotron (DESY), Hamburg, Germany, a custom-made LPBF system was used. This system was designed by Uhlmann et al.^[34] to enable the examination of LPBF parts, as they are being built layer by layer using high-energy synchrotron radiation. Thin cuboid parts were produced from 120 equally processed cp-Ti powder layers, resulting in the final part dimensions of about 21 mm in length, 2.5 mm in width, and 6 mm in height. The parts were built on titanium grade 2 substrate plates.

During the processing of the sample layer by layer, 2D diffractograms were recorded, as the sample was irradiated by the monochromatic synchrotron radiation beam in transmission mode; see **Figure 1a**. Different locations in the sample were observed to gain temporal and spatial insights into the dynamics of the thermally induced stresses and phase transformations in the bulk material. The gauge volume (GV) was positioned either at the left edge or in the center in the lateral sample direction. In the buildup direction, GV distances z_{GV} from 0 to 1 mm in the steps of 0.2 mm were observed. The GV distance z_{GV} is denoted as the distance from the GV to the working plane in which the current layer is processed; see **Figure 1b**.

For every layer, the powder bed surface was scanned by the laser with a spot size of $\approx 60\text{ }\mu\text{m}$ either longitudinally (L-Scan) or transversely (TI-Scan) regarding the incident synchrotron radiation beam; see **Figure 2**. After processing a layer, a new powder layer was deposited by an automatic powder coating mechanism. This recoating mechanism is designed to maintain a constant working distance from the laser to the powder bed.

Different parameter sets of laser power P_L and scanning speed v_L were used to study their impact on subsurface phase transformation and stress formation during the LPBF process. The transmission or longitudinal direction of the synchrotron radiation beam is denoted by LD; the layer buildup direction is denoted by BD, and the remaining axis is denoted by TD.

2.1. Evaluation of Diffraction Patterns

One of this study's main objectives is determining internal stresses during the manufacturing process utilizing high-energy X-ray diffraction. The diffraction results deliver, among other things, information regarding the lattice spacing of the

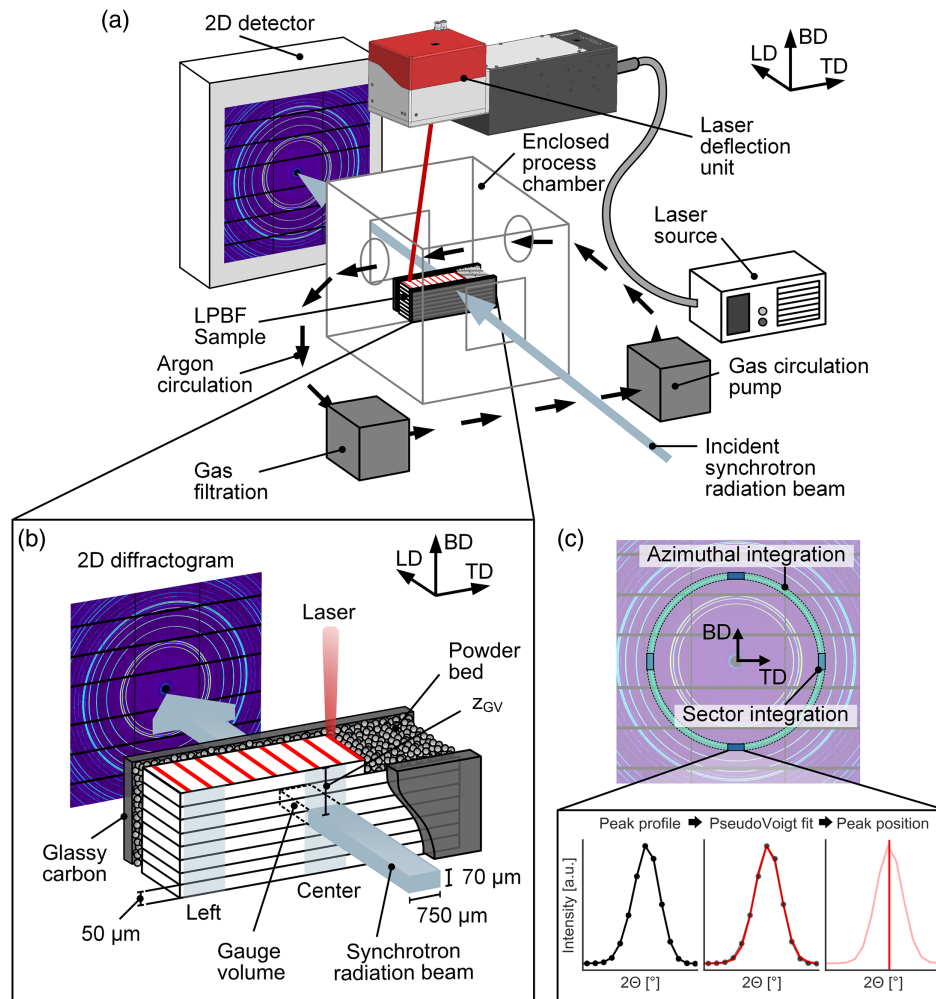


Figure 1. Schematic of the experiment: a) Experimental setup. b) Sample environment and measurement locations. c) Data evaluation.

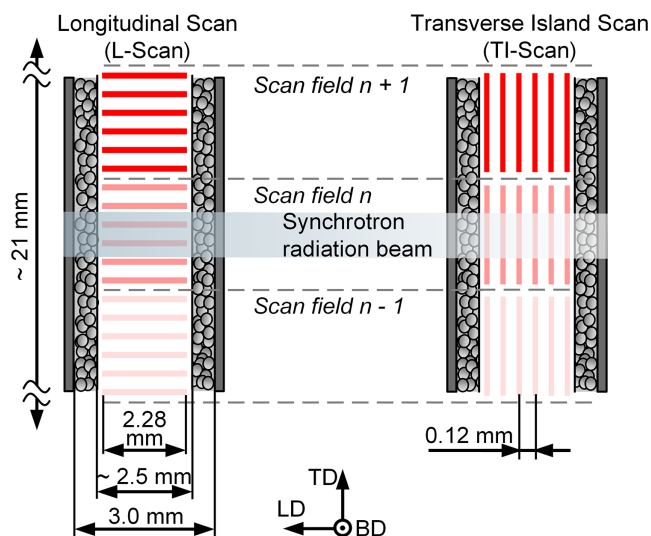


Figure 2. Scanning patterns used to fabricate samples.

crystalline material; see Figure 1c. In situ experiments using monochromatic synchrotron radiation offer several benefits: fast acquisition rates, high photon flux, and high penetration depths. A significant drawback is the lack of data in beam direction LD, which means that both strains and stresses in beam direction cannot be determined. As the stress in beam direction influences the strains in the two other normal directions, TD and BD, suitable assumptions regarding the stress state must be formulated to calculate stress values. For the given experimental setup, the parts produced had their smallest dimension in beam direction with a thickness of about 2.5 mm, whereas the width of the parts was about 21 mm, and the height was about 6 mm. Residual stresses are generally the lowest in the smallest part dimension, which is supported by simulative results by Chen et al.^[35] In addition, the substrate has about the same thickness as the parts, 3 mm, whereas its width is about 70 mm. It follows that the substrate inhibits strains in TD but not in LD, allowing the material to relax in LD. Consequently, Chen et al. found little to no deformation in thickness direction.^[35] For these reasons, a biaxial stress state is assumed where the stress in beam direction is approximated as $\sigma_{LD} = 0$ MPa. Following this boundary condition, the elastic

strains measured in the plane normal to the incident beam direction are solely the result of stresses in the same plane.

2.1.1. Stress-Free Lattice Spacing d_0

Another central prerequisite for absolute stress determination is the precise knowledge of the stress-free lattice spacing d_0 . The stress calculation is extremely sensitive to this value, and the determination of d_0 poses a challenge of its own, especially for LPBF materials.^[36,37] In this study, accurate d_0 values were gathered by collecting diffraction patterns of the primary powder material inside the process chamber under an inert gas atmosphere as part of the regular experimental procedure. The same beam apertures and exposure parameters were used to ensure consistency in the diffraction patterns.

Changes in elemental composition due to vaporization during laser-matter interaction, which would impact the stress-free lattice spacing, do not occur in cp-Ti due to the lack of alloying elements. By azimuthal integration and subsequent fitting, a room temperature stress-free lattice spacing $d_{0,\text{powd}} = 1.726280 \pm 0.000033 \text{ \AA}$ was found. Also, the room temperature lattice parameters a and c were determined by analyzing additional peaks.

2.1.2. Temperature Evaluation

The lattice spacing is influenced by both the temperature and internal stresses of the material. Decoupling these two factors is central to determine accurate internal stress values. In LPBF, the focused heat input results in steep thermal gradients and a rapidly, continuously changing temperature distribution. With the given experimental setup, temperature gradients in the GV cannot be determined. For a single diffraction pattern, a single temperature, representing the average temperature in the GV, is, therefore, used for the stress calculation.

The lattice spacings corresponding to the two principal stress directions of interest, TD and BD, are affected by the thermal strain of equal magnitude. During the laser exposure of a single

layer, the lattice spacings show a characteristic progression with a steep increase, as the laser reaches and scans over the GV, followed by a sharp decline that tapers off; see **Figure 3a**. This progression shows a maximum when the laser has reached the GV, indicating that this strain maximum coincides with the maximum temperature.

A temperature increase coincides with a reduction of the mechanical properties, especially strength. At 600°C , pure titanium's ultimate tensile strength is only 10% of its room temperature magnitude.^[38] Similarly, the yield stress decreases drastically with increasing temperature.^[39] A combination of lowered strength and high internal stress leads to plastic deformation and stress relief.

Therefore, the lattice strain at the peak d_{max} is regarded as purely thermal and allows the temperature calculation, Equation (2), via the thermal expansion, Equation (1). The observation of β reflections at the peak supports that assumption and indicates that at least parts of the GV have reached temperatures even above 882°C .

$$\varepsilon_{\text{th}} = \frac{d_{\text{max}} - d_{0,\text{powd}}}{d_{0,\text{powd}}} = \alpha \times \Delta T \quad (1)$$

$$T = 25^\circ\text{C} + \frac{1}{\alpha} \times \frac{d_{\text{max}} - d_{0,\text{powd}}}{d_{0,\text{powd}}} \quad (2)$$

The (102) lattice plane-specific coefficient of thermal expansion (CTE) was derived from the lattice parameter-dependent expansion equations reported by Medoff and Cadoff^[40] (Equation (3) and (4)).

$$a(T) = a_{\text{RT}} \times [1 + 9.928 \times (T - 25) \times 10^{-6} - 0.626 (T - 25)^2 \times 10^{-10}] \quad (3)$$

$$c(T) = c_{\text{RT}} \times [1 + 11.079 \times (T - 25) \times 10^{-6} - 9.698 (T - 25)^2 \times 10^{-10}] \quad (4)$$

As the quadratic term is four orders of magnitude smaller than the linear term, a linear approximation for the (102) CTE was used

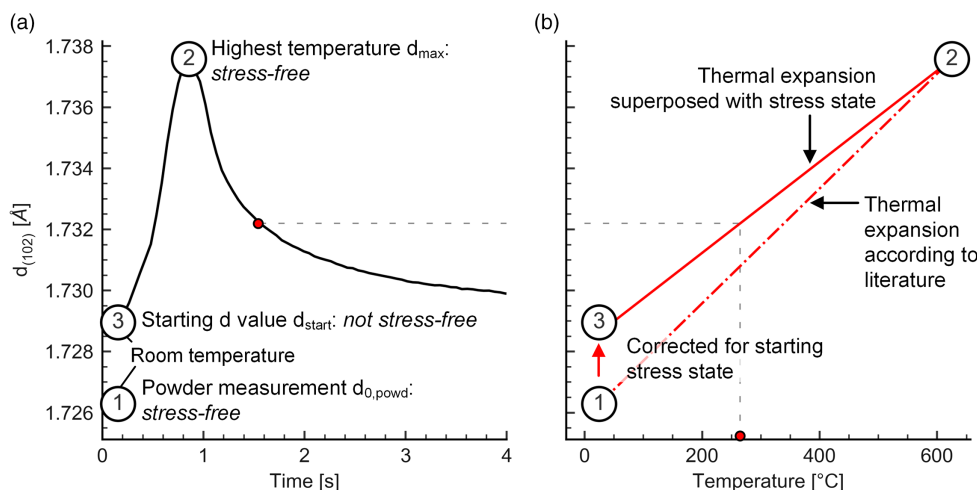


Figure 3. Temperature evaluation procedure: a) Lattice spacing progression during laser exposure. b) Temperature calculation based on characteristic lattice spacings.

and found to be equal to $\alpha(102) = 10.89 \times 10^{-6} \text{ K}^{-1}$. Using this CTE, the powder d_0 as a room temperature reference, and the peak d_{max} value in a layer, the maximum temperature for the corresponding layer was calculated based on the assumption that the material is stress-free at the peak; see Figure 3b. It was observed that the starting azimuthal d values were higher than d_0 , demonstrating tensile stresses at room temperature in the GV. Therefore, the temperature calculation was adjusted for the starting stress state by interpolating temperatures between the $d_{\text{start}}(T = 25^\circ\text{C})$ and $d_{\text{max}}(T = T_{\text{max}})$. This correction reflects the relaxation of stresses at higher temperatures. Considering this correction, the GV's temperature progression was calculated for every diffraction pattern in the sequence based on the azimuthal d values.

2.1.3. Internal Stress Calculation

The obtained temperatures were then used to calculate the stress-free lattice spacing $d_0(T)$ and the X-ray elastic constants (XECs) for each temperature. XECs are elastic constants for a specific lattice plane. They reflect the crystal anisotropy but, just like the macroscopic Young's modulus and Poisson ratio, are temperature-dependent. The temperature-dependence was derived from the single crystal moduli reported by Fisher and Renken^[41] using an Eshelby–Kröner model and linear regression.

For every diffraction pattern, a sector integration in the two assumed principal stress directions TD and BD was performed; see Figure 1c. Subsequently, stress values were calculated in two ways: stress differences between TD and BD and absolute stress values.

The stress difference is robust against uncertainties in d_0 and temperature. Also, potential stresses in LD do not affect the stress difference $\sigma_{\text{TD}} - \sigma_{\text{BD}}$. The stress difference was calculated by the following equation.

$$\sigma_{\text{TD}} - \sigma_{\text{BD}} = \frac{1}{\frac{1}{2}s_2(T)} \left[\frac{d_{\text{TD}} - d_{\text{BD}}}{d_0(T)} \right] \quad (5)$$

For calculating absolute stresses, first, the lattice strains ε_{TD} and ε_{BD} were calculated by the following equations.

$$\varepsilon_{\text{TD}} = \frac{d_{\text{TD}} - d_0(T)}{d_0(T)} \quad (6)$$

$$\varepsilon_{\text{BD}} = \frac{d_{\text{BD}} - d_0(T)}{d_0(T)} \quad (7)$$

Subsequently, the lattice strain ε_{LD} was derived from the generalized Hooke's law,^[42] Equation (8), following the premise $\sigma_{\text{LD}} = 0 \text{ MPa}$.

$$\sigma_{\text{LD}} = 0 \text{ MPa} = \frac{1}{\frac{1}{2}s_2(T)} [\varepsilon_{\text{LD}} - C \times (\varepsilon_{\text{LD}} + \varepsilon_{\text{TD}} + \varepsilon_{\text{BD}})] \quad \text{with} \quad (8)$$

$$C = \frac{s_1(T)}{\frac{1}{2}s_2(T) + 3s_1(T)} \quad (9)$$

$$\varepsilon_{\text{LD}} = \frac{C}{1 - C} (\varepsilon_{\text{TD}} + \varepsilon_{\text{BD}})$$

Absolute stress values σ_{TD} and σ_{BD} were then determined by the following equations.

$$\sigma_{\text{TD}} = \frac{1}{\frac{1}{2}s_2(T)} [\varepsilon_{\text{TD}} - C \times (\varepsilon_{\text{TD}} + \varepsilon_{\text{BD}} + \varepsilon_{\text{LD}})] \quad (10)$$

$$\sigma_{\text{BD}} = \frac{1}{\frac{1}{2}s_2(T)} [\varepsilon_{\text{BD}} - C \times (\varepsilon_{\text{TD}} + \varepsilon_{\text{BD}} + \varepsilon_{\text{LD}})] \quad (11)$$

Uncertainty evaluations are based on the standard deviation of the center parameter of the PseudoVoigt fitting function for both azimuthal and sector integrations.

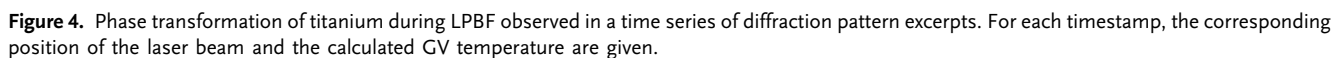
2.2. Direct Observation of High-Temperature β Phase

While a quantitative analysis of the phase transformation requires azimuthal integration and peak fitting, a look at the raw diffraction patterns provides considerable insight into some of the dynamics during the transformation. In Figure 4, a time sequence of diffraction pattern excerpts is given for a sample manufactured with a laser power of $P_L = 55 \text{ W}$ and longitudinal scanning. All the patterns show the same section of the full diffraction pattern. For each pattern, the elapsed time Δt is given, measured from the start of laser exposure. Below the diffraction pattern, a top view visualization of the sample and the laser progression is shown together with the synchrotron GV. The individual scan tracks and their relation to both the synchrotron GV in combination with the above-mentioned temperature values give an impression of the sample's thermal management.

In LPBF, the rapid laser–matter interaction results in the high cooling rates up to $10^7 \text{ }^\circ\text{C s}^{-1}$.^[43] Therefore, the phase transformation of cp-Ti is highly dynamic and occurs on short timescales but is still captured by our measurements. The first image shows the start of the layer. Only α phase reflections are visible, and the temperature is $T_{\text{GV}} = 25^\circ\text{C}$. At $\Delta t = 0.48 \text{ s}$, a weak $\beta(200)$ reflection emerges, as the calculated temperature has reached $T_{\text{GV}} = 354^\circ\text{C}$, much lower than the phase transformation temperature of 882°C . This discrepancy is caused by significant thermal gradients in the GV. While the material surrounding the laser spot, which has barely reached the synchrotron GV, is heated above the transformation temperature, the rest of the volume remains at a much lower temperature, resulting in the given calculated temperature.

The $\beta(200)$ reflection becomes more prominent in the following images and disappears again at $\Delta t = 0.86 \text{ s}$. At the same time, splitting at the $\alpha(002)/\beta(110)$ reflection is visible. These reflections have very close peak positions, because it is a shared lattice plane the phase transformation occurs at. The splitting is most prominent at $\Delta t = 0.81 \text{ s}$.

Furthermore, the emergence of a prominent β spot is visible once the GV temperature reaches $T_{\text{GV}} = 613^\circ\text{C}$ at $\Delta t = 0.70 \text{ s}$. The spot's orientation and intensity slightly change, as the laser moves over the GV. The temperature threshold for the β spot to disappear was $T_{\text{GV}} = 382^\circ\text{C}$ at $\Delta t = 1.08 \text{ s}$. Therefore, this large β spot was stable for about 0.4 s , implying that at least part of the GV had a temperature above the phase transformation temperature of 882°C for that time. The difference in temperatures between the spot's appearance and vanishing shows the delay of heat conduction inside the synchrotron GV. While the



It is important to note that the GV for Figure 4 is positioned 200 μm below the surface of the powder bed to observe previously solidified layers. Therefore, this figure is a visual example that, during LPBF, it is not only the powder layer that experiences the phase transformation during melting and cooling. Even three layers below the surface, in this case, the material reaches the transformation temperature. However, the data do not show that all of the GV reaches the transformation temperature simultaneously or has a constant temperature. The diffraction patterns represent an integrated result over all the grains in the GV. Temperature gradients in the GV cannot be depicted directly.

Figure 5 compares the effect of the two different scanning patterns on the peak shift for a laser power $P_L = 55$ W. For each scanning pattern, different GV positions z_{GV} with increasing distance to the powder bed's top surface are shown. For the distance $z_{GV} = 0$ μm , the GV was located in the currently processed powder layer, whereas a distance $z_{GV} = 200$ μm equals three layers beneath the currently processed powder layer. While raw diffraction data were analyzed in the previous section, diffraction patterns were fully azimuthally integrated to show the diffracted peaks' progression during the laser exposure of a single layer here.

Figure 5a shows the phase transformation most clearly. As the laser scans over the GV, a peak shift to lower diffraction angles is visible first before the α peaks vanish completely, and only β peaks remain. The peak shift represents a lattice expansion

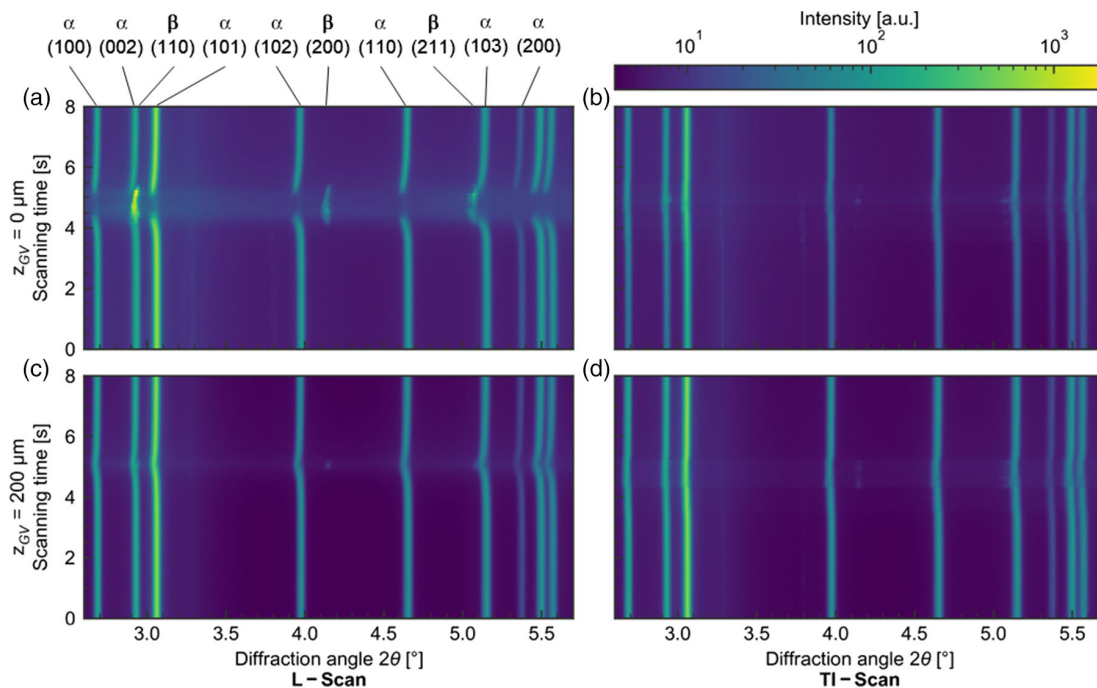


Figure 5. Peak shift during laser exposure for two scanning strategies, both exposed with $P_L = 55$ W and synchrotron GV placed in the center of the sample. a,c) L-Scan samples with increasing depth of the GV, starting in the powder layer down to $200\ \mu\text{m}$ below. b,d) The corresponding TI-Scan samples.

due to increasing temperature. The β peaks also show a lattice expansion and subsequently decrease, as they shift to the left and then back right before vanishing. For the L-Scan, β peaks were observed in the solidified material for $z_{GV} = 200\ \mu\text{m}$ below the top surface. Intensity counts for the β phase are a lot lower, and their presence is also much shorter. Furthermore, both α and β coincide in the solidified material, as not all the material in the measured volume is transformed, i.e., reaches the phase transformation temperature of $882\ ^\circ\text{C}$.

For the TI-Scan, the β peaks were a lot less pronounced than for the L-Scan, which is likely caused by the geometrical relation between scanning vectors and synchrotron GV. The GV has a width of $700\ \mu\text{m}$ and a depth of $3\ \text{mm}$. In TI scanning, the GV is traversed 19 times by the laser, each pass only lasting for about $0.014\ \text{s}$ for $v_L = 50\ \text{mm s}^{-1}$. This scanning pattern results in significantly lower β intensities than L scanning, where the GV's full depth is traversed by a single laser hatch, thus showing β reflections for a comparatively longer duration.

In a distance of $z_{GV} = 200\ \mu\text{m}$ to the top surface, the β peaks were visible but weak for the TI-Scan. They appeared for a longer duration than for the L-Scan, though, which results from the scanning pattern. In all four plots, diffuse scattering during the laser scan is present but most pronounced in the top left plot. It may indicate the presence of a liquid phase, which is expected for the top layer but not necessarily for the layers below.

While the single layers chosen to be presented in Figure 5 are considered representative, a quantitative analysis of the whole process is carried out. Each GV was observed for a total of 20 layers. For those 20 layers, the occurrence of β peaks was

counted. All samples showed β reflections up to a depth of $z_{GV} = 200\ \mu\text{m}$. For TI-scanned samples, β reflections occurred up to a distance to the powder layer of $z_{GV} = 400\ \mu\text{m}$, but only in 10% of the observed layers for $P_L = 55\ \text{W}$ and 15% of the layers for $P_L = 275\ \text{W}$. Below $400\ \mu\text{m}$, no β reflections were visible for either sample. Hence, it can be deduced that phase transformations during the processing of titanium appear up to seven layers beneath the currently processed powder layer for the given process parameters.

2.4. Parameter-Dependent Residual Stress Buildup

Further analysis of the diffraction patterns was performed to determine stresses during manufacturing. The diffraction patterns were segmented into sectors to determine directional lattice spacings in TD and BD that were subsequently converted into lattice strains. The strain difference between TD and BD was used to calculate the respective stress difference described in Section 2.1.3.

For the $\alpha(102)$ reflection, the median stress difference $\Delta\sigma = \sigma_{TD} - \sigma_{BD}$ was calculated, depending on the GV's lateral and vertical position as well as the process parameters used to fabricate the sample; see Figure 6. Each data point in the figure represents the median stress difference for all the diffraction patterns collected over 20 layers in the respective GV.

Schmeiser et al. showed the formation of a subsurface stress maximum during LPBF for Inconel 625 and a single sample.^[8] In the center of the sample and about $350\ \mu\text{m}$ below the top surface, the maximum stress difference $\Delta\sigma$ was found. The results presented in Figure 6 expand upon the results from Schmeiser

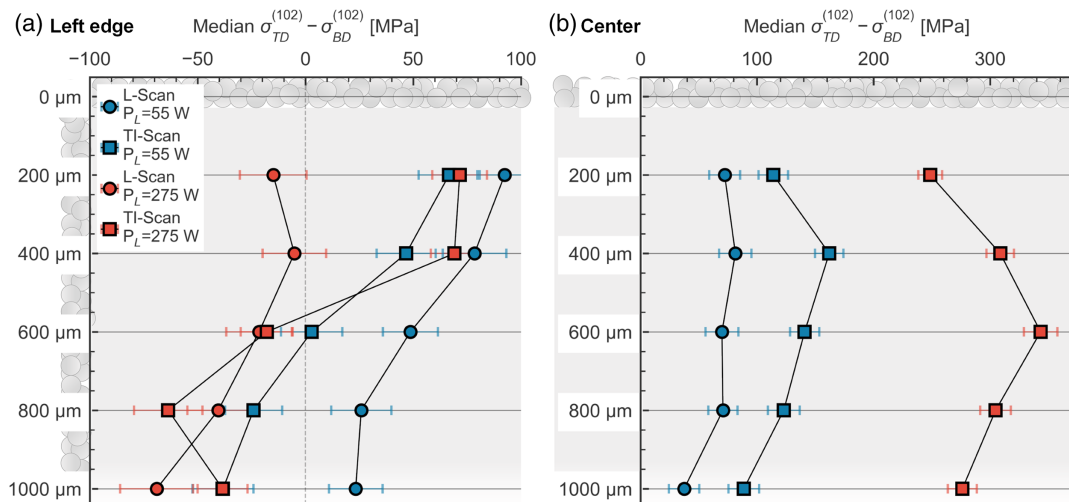


Figure 6. Median stress difference $\sigma_{TD} - \sigma_{BD}$ for a) left edge and b) center GV positions and different sets of process parameters.

et al. They show a maximum stress difference in the center of the sample as well. The magnitude and position of this maximum vary with the process parameters. A higher laser power P_L leads to a shift into deeper layers away from the sample surface, caused by the heat-affected zone's (HAZ) higher penetration depth.

Furthermore, the impact of the scanning strategy is apparent. The stress values for TI-scanned samples are higher than those processed by L-Scan. Both the highest stress difference of about 340 MPa and the deepest maximum position at $z_{GV} = 600$ μm were found for the TI-scanned sample with a laser power of $P_L = 275$ W.

At the left edge of the sample, where the laser exposure begins each layer, all parameters show a similar gradient with increasing depth. Except for the L-scanned sample with $P_L = 275$ W, all parameter sets started with a positive stress difference. Here, the solidified material's hindered contraction through the temperature gradient mechanism (TGM) is the stress-inducing mechanism. Another effect can be seen with increasing distance to the surface, as the stress difference is inverted into compression for three out of four parameter sets.

This inversion indicates that with greater distance to the surface, BD stresses are greater than in TD. Phan et al.^[44] performed ex situ measurements on additively manufactured components with comparable geometry to this study's parts. They found a similar inversion at the edge of their sample, where the absolute directional strains changed from tensile to compressive in TD and the opposite for BD. Following these results, the inversion of the stress difference found in this study could also indicate that tensile stresses occur in BD and compressive stresses in TD in deeper layers.

This stress inversion compensates for the reversed stress state in the center of the sample, where tensile stresses in TD and compressive stresses in BD are expected. It has to be noted that due to the experimental procedure, the lower z_{GV} values were investigated first for every sample. Hence, stresses for the lower z_{GV} values experience a more substantial influence by the substrate, such as its stress state and the first layer's bonding to the substrate.

The discrepancies between the sample's left edge and the center vary depending on the scanning strategy and laser power. For samples produced with L-Scan and low laser power, both measurement locations' progressions were very similar. That implies that a homogeneous stress state can be generated with these manufacturing parameters. On the other hand, the stress progressions in the two measuring locations varied distinctly for TI-scanned samples. The discrepancy between the sample edge and the center is highest for samples produced using TI scanning with high laser power.

2.5. Subsurface Stress Progression in a Single Layer

Figure 7a shows the stress progression corresponding to the diffraction patterns in Figure 4 and the estimated average temperature in the GV. As the laser scans over the left edge GV, the GV's maximum temperature is reached. With the given data analysis, a peak temperature of $T_{GV} = 625$ °C was estimated. In Figure 4, the beta phase occurrence indicated that at least part of the GV had to have reached the phase transformation temperature of 882 °C, which is higher than the peak temperature estimated here. The difference is accounted for by the size of the irradiated volume. The larger the analyzed volume, the lower the average temperature. The beta phase only occurs directly around the laser spot, which has a diameter of just ≈ 60 μm. The volume used for the temperature calculation is more extensive than the part surrounding the laser spot and, therefore, averages large thermal gradients, resulting in a lower peak temperature. Despite the apparent temperature gradients in the GV, an average temperature is a valuable measure to calculate absolute stress values in the whole GV. Determining individual grains' temperatures and stresses from a single diffraction pattern is not feasible with the given experimental setup.

In addition, Figure 7b shows the temperature and stress progression for the same process parameters with the GV located in the sample center. Here, a higher peak temperature of about $T_{GV} = 665$ °C is reached.

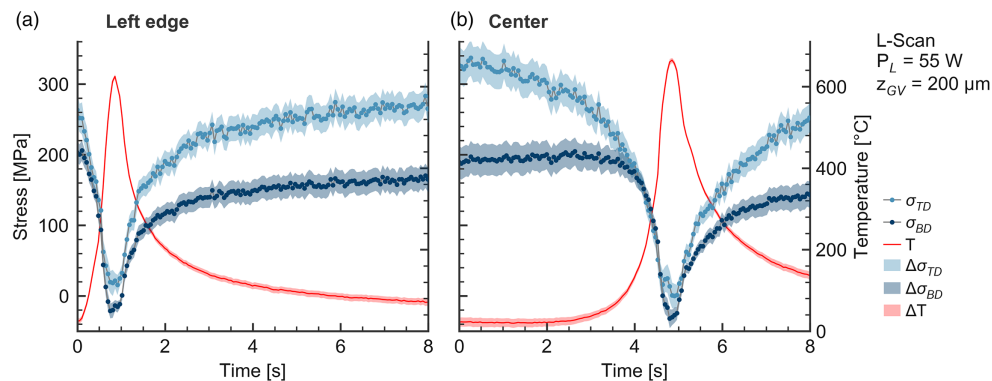


Figure 7. Absolute stress estimation for a single subsurface layer while the laser passes over the GV with a laser power of $P_L = 55$ W, L-Scan pattern, and $z_{GV} = 200 \mu\text{m}$: a) GV located at the left edge of the sample and b) GV in the center of the sample.

Before the laser reaches the GV and the temperature increases sharply, tensile stresses in TD and BD were found, with $\sigma_{TD} = 265$ MPa being about 60 MPa higher than $\sigma_{BD} = 205$ MPa in the left edge GV and about 140 MPa higher in the center GV with $\sigma_{TD} = 320$ MPa and $\sigma_{BD} = 180$ MPa. This stress difference supports the TGM model by Mercelis and Kruth^[7] and transverse contraction elaboration by Schmeiser et al.^[8] As the temperature increases, the stresses drop due to a reduction of the material's stiffness. The material's yield strength has decreased significantly at the temperature peak, leading to plastic deformation and reducing stresses to almost zero.

After the peak temperature is reached, the stresses increase, as the material cools down and its stiffness increases. Simultaneously, the laser has scanned the powder above the GV, and as the molten powder solidifies, it shrinks. The material below, including the GV, impedes that contraction, which induces tensile stresses in the GV. Eventually, the TD stresses reach similar levels as before the peak temperature in Figure 7a with $\sigma_{TD} = 260$ MPa, whereas BD stresses reach $\sigma_{BD} = 160$ MPa, about 40 MPa less than before the laser impact, which is an indication of transverse contraction. In Figure 7b, the stresses appear to be lower after the temperature peak with $\sigma_{TD} = 250$ MPa and $\sigma_{BD} = 140$ MPa. It should be noted that this might be caused by the experimental procedure, as the material has not cooled to the same degree as in Figure 7a during the observation period, implying that further stress increase could happen.

3. Conclusion

A comprehensive study to investigate the subsurface phase transformation and formation of internal stresses in additively manufactured commercially pure titanium grade 1 was carried out at the P07 high energy materials science (HEMS) beamline at the synchrotron facility PETRA III. A custom LPBF machine was used to conduct the experiments. It was shown that the α - β phase transformation occurs in subsurface layers and during initial melting and solidifying. Depending on the process parameters, β titanium reflections were found to a depth of $400 \mu\text{m}$ or seven layers below the surface. Furthermore, the previously reported formation of a stress difference maximum below the surface was confirmed and elaborated. The results show that

higher laser powers lead to a shift of the stress difference maximum into deeper layers. At the samples' left edge, a stress inversion was found with increasing distance to the top surface. A lower laser power leads to more homogeneous stress distribution in the sample. For the first time in LPBF, absolute in situ stress values are calculated, considering temperature and stress state. During laser impact, the stress values decrease rapidly due to a reduction in stiffness. During cooling, they reach their previous magnitude.

4. Experimental Section

Modified LPBF System: The experimental LPBF system used in this study was described in the previous work.^[34] It was equipped with a 400 W ytterbium fiber laser YLR-400-AC from IPG Laser GmbH, Burbach, Germany. The collimated laser beam with a wavelength of 1070 nm was directed and focused onto the powder bed via a three-axis deflection unit Axialscan-30 from Raylase GmbH, Wessling, Germany, with a laser focus diameter of $\approx 60 \mu\text{m}$ ($1/e^2$). The powder bed was enclosed in a gas-tight process chamber, with a size that allows for parts of up to $3 \text{ mm} \times 70 \text{ mm} \times 10 \text{ mm}$. The powder bed limitations were made from glassy carbon and acted as X-ray transmissive windows. Also, the process chamber housing contained polyimide windows guaranteeing X-ray transmission through the process chamber. Before the experiments, the chamber was purged with argon to prevent oxidation during the processing. The inert gas atmosphere was continuously circulated and filtered to ensure that the welding fumes do not lead to a loss of laser radiation intensity. An installed recoating mechanism allowed for automatic powder recoating and, therefore, the manufacturing of multilayer parts.

Materials: The titanium powder used in this study was supplied by Advanced Powders & Coatings, Quebec, Canada. It conformed to ASTM B348 grade 1 in terms of its composition. The particles were spherical, and the particle size distribution was between 20 and $63 \mu\text{m}$ with a 90th percentile $D_{90} = 54 \mu\text{m}$. The substrates were manufactured from commercially pure titanium grade 2.

LPBF Process Parameters and Measurement Modes: The LPBF process parameters used in this study are listed in Table 1. A laser power of $P_L = 55 \text{ W}$ yielded acceptable density results with a relative density of $\rho_r > 99.0\%$ compared with conventionally produced titanium with a density of $\rho = 4.5 \text{ g cm}^{-3}$. Parameter sets 1 and 3 offered high temporal resolution for the diffraction experiments, whereas sets 2 and 4 contained the laser power value $P_L = 275 \text{ W}$ of an industrially used parameter set for dense parts with a compromise in temporal resolution. Two different scanning patterns were investigated. For the longitudinal scanning (L-Scan), only unidirectional scanning vectors, without meandering, parallel to

Table 1. Process parameters.

| Parameter | Unit | Set 1 | Set 2 | Set 3 | Set 4 |
|-----------------------------|--------------------|-------|-------|-------|-------|
| Laser power, P_L | W | 55 | 275 | 55 | 275 |
| Scanning speed, v_L | mm s ⁻¹ | 50 | 760 | 50 | 760 |
| Scanning pattern | | L | L | TI | TI |
| Laser spot diameter, d_L | μm | | ≈60 | | |
| Hatch distance, h_L | μm | | 120 | | |
| Layer thickness, Δz | μm | | 50 | | |

the primary synchrotron radiation beam were utilized. For the transverse island scanning (TI-Scan), the scanning vectors were transverse to the synchrotron radiation beam with vector lengths of the same magnitude as for the L-Scan vectors. Hence, several vector fields or islands were formed over the scan layer; see Figure 1a.

Measurements were conducted in measurement mode 1 (MM1).^[34] In MM1, the GV was in a defined distance z_{GV} to the topmost layer, the working plane. After processing of a layer, the sample was moved in negative BD by the amount of the layer thickness Δz , whereas the glassy carbon plates and the working plane stayed on a constant BD level. Then, a new powder layer was deposited, and the procedure was repeated. Accordingly, relative to the sample, the GV's vertical position along BD changed layer by layer, whereas the lateral position, along TD, was fixed throughout the buildup of one sample.

In any individual sample, the GV distance to the top surface z_{GV} , Figure 1b, was kept constant for 20 layers. Afterward, the distance z_{GV} was increased by 200 μm, and the process was repeated for another 20 layers. In total, six values for z_{GV} were investigated for each sample from 0 to 1000 μm. For each parameter set, two lateral GV locations were observed: the left edge of the sample and the center of the sample.

In Situ Diffraction Experiments: In situ high energy synchrotron radiation diffraction experiments were carried out at the HEMS beamline P07 at PETRA III at DESY, Hamburg, Germany.^[33] A beam energy of $E = 103.43$ keV ($\lambda = 0.1199$ Å) was used. The X-ray beam size was set to 700×100 μm to reach a satisfactory spatial resolution in the build direction. The width of the GV was adjusted to irradiate enough grains to collect full diffraction patterns.

Diffraction patterns were collected using a Dectris PILATUS3 2M detector using a sampling rate of $f = 20$ Hz for measurements in solidified material and $f = 10$ Hz when measuring in the powder layer. The distance between sample and detector was 1110.237 mm to collect the first 13 αhkl reflections. Lanthanum hexaboride (LaB₆) was used to determine the sample-to-detector distance. Subsequently, the diffraction patterns were azimuthally integrated using the python library pyFAI.^[45] For the phase transformation results, full integration was performed, whereas a sector integration was used for stress results. For the sector integration, the diffraction rings were divided into 72 equal-angle sectors.

The integration produced 1D line spectra, where the (102) reflection was approximated employing a PseudoVoigt function using the python library lmfit.^[46] The (102) reflection was chosen for stress analysis due to several advantages: its distance to neighboring peaks, absence of overlap with β peaks, and preferable location on the Pilatus detector's tiles.

Sector integration yielded the lattice spacings in TD and BD, where d_{TD} corresponded to the averaged peak position gathered from the sectors with azimuths $\eta = 0^\circ$ and $\eta = 180^\circ$, whereas d_{BD} was related to the peak positions from sectors parallel to BD, azimuths $\eta = 90^\circ$ and $\eta = 0^\circ$.

Acknowledgements

This article was based on the results obtained in project No. 317078200 supported by the Deutsche Forschungsgemeinschaft (DFG). Furthermore, the authors acknowledge Helmholtz-Zentrum Hereon (HZH) for the

support and the provision of experimental facilities at PETRA III. They also thank the three anonymous reviewers for their thorough and extensive comments, thereby improving this manuscript substantially.

Open access funding enabled and organized by Projekt DEAL.

Conflict of Interest

The authors declare no conflict of interest.

Data Availability Statement

The data that support the findings of this study are available from the corresponding author upon reasonable request.

Keywords

commercially pure titanium, in situ synchrotron radiation diffraction, internal stress, laser powder bed fusion, phase transformation, subsurface

Received: December 18, 2020

Revised: March 16, 2021

Published online: June 4, 2021

- [1] M. Seifi, A. Salem, J. Beuth, O. Harrysson, J. J. Lewandowski, *JOM* **2016**, 68, 747.
- [2] L.-C. Zhang, H. Attar, M. Calin, J. Eckert, *Mater. Technol.* **2016**, 31, 66.
- [3] L. Parry, I. A. Ashcroft, R. D. Wildman, *Addit. Manuf.* **2016**, 12, 1.
- [4] G. Mohr, S. J. Altenburg, K. Hilgenberg, *Addit. Manuf.* **2020**, 32, 101080.
- [5] G. Mohr, N. Scheuschner, K. Hilgenberg, *Procedia CIRP* **2020**, 94, 155.
- [6] Y. Li, D. Gu, *Addit. Manuf.* **2014**, 1–4, 99.
- [7] P. Mercelis, J.-P. Kruth, *Rapid Prototyp. J.* **2006**, 12, 254.
- [8] F. Schmeiser, E. Krohmer, N. Schell, E. Uhlmann, W. Reimers, *Addit. Manuf.* **2020**, 32, 101028.
- [9] J. L. Bartlett, X. Li, *Addit. Manuf.* **2019**, 27, 131.
- [10] Z.-C. Fang, Z.-L. Wu, C.-G. Huang, C.-W. Wu, *Opt. Laser Technol.* **2020**, 129, 106283.
- [11] Z. Xiao, C. Chen, H. Zhu, Z. Hu, B. Nagarajan, L. Guo, X. Zeng, *Mater. Des.* **2020**, 193, 108846.
- [12] T. Mukherjee, V. Manvatkar, A. De, T. DebRoy, *Scr. Mater.* **2017**, 127, 79.
- [13] H. Ali, H. Ghadbeigi, K. Mumtaz, *J. Mater. Eng. Perform.* **2018**, 27, 4059.
- [14] N. C. Levkulich, S. L. Semiatin, J. E. Gockel, J. R. Middendorf, A. T. DeWald, N. W. Klingbeil, *Addit. Manuf.* **2019**, 28, 475.
- [15] F. R. Kaschel, M. Celikin, D. P. Dowling, *J. Mater. Process. Technol.* **2020**, 278, 116539.
- [16] A. S. Wu, D. W. Brown, M. Kumar, G. F. Gallegos, W. E. King, *Metall. Mater. Trans. A* **2014**, 45, 6260.
- [17] Y. Liu, Y. Yang, Di Wang, *Int. J. Adv. Manuf. Technol.* **2016**, 87, 647.
- [18] J. Robinson, I. Ashton, P. Fox, E. Jones, C. Sutcliffe, *Addit. Manuf.* **2018**, 23, 13.
- [19] J.-P. Kruth, J. Deckers, E. Yasa, R. Wauthlé, *Proc. Inst. Mech. Eng. B* **2012**, 226, 980.
- [20] I. Yadroitsava, S. Grewar, D. Hattingh, I. Yadroitsev, *Mater. Sci. Forum* **2015**, 828–829, 305.
- [21] H. Ali, H. Ghadbeigi, K. Mumtaz, *Mater. Sci. Eng., A* **2018**, 712, 175.
- [22] J. C. Williams, R. R. Boyer, *Metals* **2020**, 10, 705.

- [23] P. Bartolo, J.-P. Kruth, J. Silva, G. Levy, A. Malshe, K. Rajurkar, M. Mitsuishi, J. Ciurana, M. Leu, *CIRP Ann.* **2012**, 61, 635.
- [24] A. Kolomiets, Y. J. Grobman, V. V. Popov, E. Strokin, G. Senchikhin, E. Tarazi, *J. New Music Res.* **2020**, 760, 1.
- [25] U. Zwicker, *Titan und Titanlegierungen*, Springer, Berlin, Heidelberg **1974**.
- [26] D. Gu, Y.-C. Hagedorn, W. Meiners, G. Meng, R. J. S. Batista, K. Wissenbach, R. Poprawe, *Acta Mater.* **2012**, 60, 3849.
- [27] H. Attar, M. Calin, L. C. Zhang, S. Scudino, J. Eckert, *Mater. Sci. Eng., A* **2014**, 593, 170.
- [28] B. Attard, S. Cruchley, C. Beetz, M. Megahed, Y. L. Chiu, M. M. Attallah, *Addit. Manuf.* **2020**, 36, 101432.
- [29] N. P. Calta, V. Thampy, D. R. Lee, A. A. Martin, R. Ganeriwala, J. Wang, P. J. Depond, T. T. Roehling, A. Y. Fong, A. M. Kiss, C. J. Tassone, K. H. Stone, J. Nelson Weker, M. F. Toney, A. W. van Buuren, M. J. Matthews, *Mater. Des.* **2020**, 195, 108987.
- [30] S. Hocine, H. van Swygenhoven, S. van Petegem, C. S. T. Chang, T. Maimaitiyili, G. Tinti, D. Ferreira Sanchez, D. Grolimund, N. Casati, *Mater. Today* **2020**, 34, 30.
- [31] C. Zhao, K. Fezzaa, R. W. Cunningham, H. Wen, F. de Carlo, L. Chen, A. D. Rollett, T. Sun, *Sci. Rep.* **2017**, 7, 3602.
- [32] D. Dye, H. J. Stone, M. Watson, R. B. Rogge, *Metall. Mater. Trans. A* **2014**, 45, 2038.
- [33] N. Schell, A. King, F. Beckmann, T. Fischer, M. Müller, A. Schreyer, *Mater. Sci. Forum* **2013**, 772, 57.
- [34] E. Uhlmann, E. Krohmer, F. Schmeiser, N. Schell, W. Reimers, *Rev. Sci. Instrum.* **2020**, 91, 75104.
- [35] C. Chen, Z. Xiao, H. Zhu, X. Zeng, *Int. J. Adv. Manuf. Technol.* **2020**, 110, 3467.
- [36] Z. Wang, E. Denlinger, P. Michaleris, A. D. Stoica, D. Ma, A. M. Beese, *Mater. Des.* **2017**, 113, 169.
- [37] T. Mishurova, I. Serrano-Muñoz, T. Fritsch, A. Ulbricht, M. Sprengel, A. Evans, A. Kromm, M. Madia, G. Bruno, in *Structural Integrity of Additive Manufactured Materials & Parts* (Eds.: N. Shamsaei, M. Seifi), ASTM International, West Conshohocken, PA **2020**, p. 122.
- [38] J. W. Suiter, *J. Inst. Met.* **1954/55**, 6, 460.
- [39] S. Nemat-Nasser, W. G. Guo, J. Y. Cheng, *Acta Mater.* **1999**, 47, 3705.
- [40] J. I. Medoff, I. Cadoff, *J. Met.* **1959**, 11, 581.
- [41] E. S. Fisher, C. J. Renken, *Phys. Rev.* **1964**, 135, 482.
- [42] V. Hauk, H. Behnken, *Structural and Residual Stress Analysis by Nondestructive Methods: Evaluation – Application – Assessment*, Elsevier, Amsterdam **1997**.
- [43] U. Scipioni Bertoli, G. Guss, S. Wu, M. J. Matthews, J. M. Schoenung, *Mater. Des.* **2017**, 135, 385.
- [44] T. Q. Phan, M. Strantz, M. R. Hill, T. H. Gnaupel-Herold, J. Heigel, C. R. D'Elia, A. T. DeWald, B. Clausen, D. C. Pagan, J. Y. Peter Ko, D. W. Brown, L. E. Levine, *Integr. Mater. Manuf. Innov.* **2019**, 8, 318.
- [45] G. Ashiotis, A. Deschildre, Z. Nawaz, J. P. Wright, D. Karkoulis, F. E. Picca, J. Kieffer, *J. Appl. Crystallogr.* **2015**, 48, 510.
- [46] M. Newville, T. Stensitzki, D. B. Allen, A. Ingargiola, *LMFIT: Non-Linear Least-Square Minimization and Curve-Fitting for Python*, Zenodo.